Mechanical properties of Hastelloy X produced by laser powder bed fusion and affected by spatter redeposition

Journal of Materials Research and Technology 29 (2024) 4200–4215

Contents lists available at ScienceDirect

Journal of Materials Research and Technology

journal homepage: www.elsevier.com/locate/jmrt

Mechanical properties of Hastelloy X produced by laser powder bed fusion and affected by spatter redeposition

Claudia Schwerz [a,*], Johan Moverare [b], Vishal Sundar [a], Benjamin A. Bircher [c], Alain Küng [c], Dmitri Riabov [a,d], Lars Nyborg [a]

[a] Chalmers University of Technology, Department of Industrial and Material Science, Sweden
[b] Linköping University, Department of Management and Engineering, Sweden
[c] Federal Institute of Metrology METAS, Laboratory for Length, Nano- and Microtechnology, Switzerland
[d] Höganäs AB, Sweden

ARTICLE INFO

Handling editor: SN Monteiro

Keywords:
In-situ monitoring
Defects
Spatter
Productivity
Fatigue
X-ray computed tomography

ABSTRACT

Defects in materials manufactured via laser powder bed fusion challenge this manufacturing process' dependability and may prevent it from being comprehensively used for structural components, particularly those intended to operate under dynamic loading conditions. This study aims to investigate the effect of spatter-driven lack of fusion on the mechanical properties of Hastelloy X, with a particular focus on fatigue performance. Mechanical test specimens were manufactured in two builds with different build rates and monitored through in-situ optical tomography. The images acquired in situ were analyzed to detect spatter redeposits to predict the defect content in the gauge section. Selected specimens were measured ex-situ using X-ray computed tomography to map the defect populations. Afterward, the specimens were tensile and fatigue tested, and their performance was analyzed based on the measured and expected defect populations. It was confirmed that a higher build rate is associated with more extensive detection of spatter redeposits in optical tomography images and lack of fusion defects. The fatigue lives of specimens manufactured at higher build rates presented higher scatter but significantly higher average, despite the more critical defect population. Surprisingly, the confirmed presence of lack of fusion defects in the gauge section of test specimens did not necessarily result in a poorer fatigue performance. It was concluded that the grain refinement obtained through the increase in nominal layer thickness has a life-prolonging effect that overrides the effects of spatter-induced lack of fusion defects.

1. Introduction

The industrial application of laser powder bed fusion (LPBF) is still limited. Even though the resistance to its adoption depends on the specificities of the intended applications, commonly cited obstacles are low productivity [1,2] and associated high cost, and reliability concerns [3,4].

The resistance faced based on reliability is particularly important concerning structural integrity and mechanical performance [5]. While LPBF materials generally perform satisfactorily in static loading conditions thanks to their fine microstructure, their performance under dynamic loading can be significantly inferior to their traditionally manufactured counterparts [6]. In particular, scatter in fatigue properties is an often observed issue in additively manufactured materials and is largely attributed to defects [7,8]. A factor that can prompt the appearance of defects in LPBF is spatters, unavoidable process by-products consisting of oxidized metal particles. In the event these particles, formed in-process, land on a part of ongoing manufacturing, a complete metallurgical bond might be hindered, hence causing lack of fusion (LoF) defects [9–11]. These defects tend to be large, with sizes in the order of several hundreds of micrometers [11,12], thus particularly critical, as defect size is a major driver of fatigue performance even in additively manufactured materials [13].

To overcome the limitations related to productivity issues, machine manufacturers have been developing strategies such as the implementation of multiple heat sources for the simultaneous processing of multiple regions of the powder bed [14], and modification of the laser beam profile for optimized heat transfer to the powder bed [15]. The process productivity can also be enhanced by simpler, readily available means, e.g., through the selection of processing parameters [16,17].

* Corresponding author.
E-mail addresses: claudia.schwerz@chalmers.se, cschwerz@outlook.com (C. Schwerz).

https://doi.org/10.1016/j.jmrt.2024.02.150
Received 14 December 2023; Received in revised form 31 January 2024; Accepted 19 February 2024
Available online 21 February 2024

Notably, the nominal layer thickness is one of the main factors driving productivity, thanks to the linear relationship between these variables [18].

When the process limits are pushed towards conditions that allow higher productivity, the integrity of the manufactured parts might be compromised. The surface quality [1,15] and geometrical accuracy [19] are some of the factors affected, but also the formation of internal, stochastic defects [11]. Larger quantities of spatter are formed when multiple lasers operate [20] and when the instant energy input is increased [21,22], both processing conditions that increase productivity. The spattering phenomenon is also magnified with the use of larger nominal layer thicknesses [23]. With a larger quantity of spatters generated per layer [24] combined with a smaller remelt ratio, lack of fusion defects in larger numbers and sizes are generated [12], as the surface oxidation and size typical of these particles induce defect formation [25,26].

This work addresses two major and correlated shortcomings of LPBF combined: spatter-driven defects and productivity, specifically, how the increased productivity impacts defect formation and mechanical properties. For that, mechanical test specimens are manufactured in geometrically identical builds with two different nominal layer thicknesses, hence productivities. Specimens manufactured at three locations on the build platform are selected for tensile testing. Other specimens manufactured across the build area are surface treated and tested in fatigue to evaluate the effect of internal defects. The build processes are monitored in-situ via optical tomography (OT), from which the presence of defects can be inferred. A few specimens were also selected for X-ray computed tomography, where the presence of defects inferred from OT images can be confirmed.

2. Materials and methods

2.1. Laser powder bed fusion manufacturing

Mechanical test specimens were manufactured in a M290 (EOS GmbH) laser powder bed fusion machine according to the layout shown in Fig. 1, in which 36 identical specimens were laid on a 3 × 12 grid centered on the *x*-axis. Two build jobs were performed for this study, using identical processing conditions, except for the nominal layer thickness, which was 80 μm for build 1, and 120 μm for build 2. This processing parameter was varied as it has been identified as a major factor simultaneously driving spatter-induced defects [11] and process productivity [18]. Indeed, the build times were 22 h 49 min, and 15 h 35 min for builds 1 and 2, respectively. The sets of specimens manufactured in builds 1 and 2 will henceforth be referred to as set 1 and set 2.

The processing conditions, presented in Table 1, were selected to produce virtually defect-free bulk material, i.e., minimal porosity and no cracks. The employed parameters were verified in previous work and yielded defect contents of less than 0.05% for both nominal layer thicknesses [12]. An EOS grid nozzle was used to allow argon gas flow into the build chamber. The feedstock powder was argon gas atomized Amperprint ® 0228 Hastelloy X from Höganäs AB, with nominal particle size range of 15 μm–45 μm and nominal composition as per Table 2.

2.2. LPBF process monitoring and detection of spatter redeposits

The M290 machine is equipped with EOSTATE OT (EOS GmbH), a monitoring system containing a sCMOS (scientific complementary metal-oxide-semiconductor) camera installed externally on the top of the build chamber. A narrow (25 nm) bandpass filter centered on 900 nm is installed on the camera, which continuously acquires images of the entire build area during the exposure of a print layer, with an exposure time of 0.1s. The images acquired during the processing of a single print layer are combined within the system, generating two outputs of dimensions 2000 × 2000 pixels: the maximum intensity on regions of size 125 μm × 125 μm (*MAX* output), and the integral intensities in each of these regions (*INT* output). Geometrical and intensity corrections are applied. EOSTATE OT was used for data acquisition only;

Table 1
Process parameters used in the manufacturing of specimens in sets 1 and 2.

Build ID	Set 1	Set 2
Nominal layer thickness (μm)	80	120
Nominal laser power (W)	370	
Laser spot size (μm)	100	
Laser scan speed (mm/s)	1000	
Hatch spacing (μm)	100	
Scan pattern	Stripes with 67° rotation between consecutive layers	
Build plate preheat temperature	80 °C	
Process atmosphere	Argon, with maximum allowed oxygen content 1000 ppm	

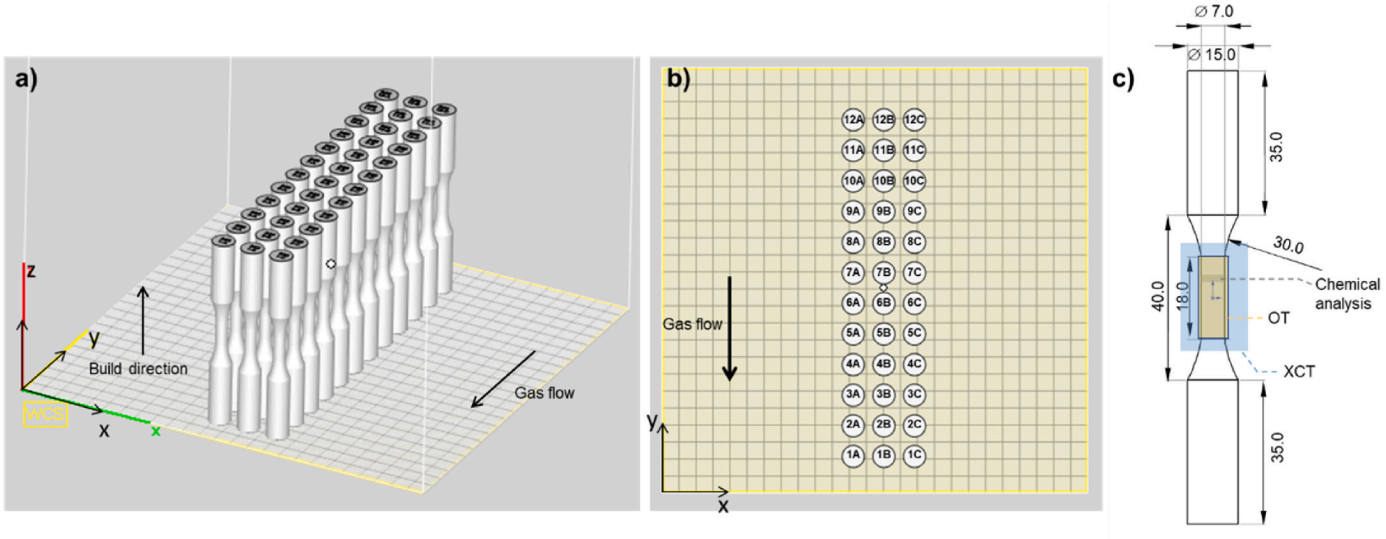

Fig. 1. a) Build layout, isometric view; b) top view with specimen identification. Geometry and nominal dimensions of the as-printed specimens (c), highlighting the XCT (in blue), OT (in yellow), and bulk chemistry (in grey) analyses regions. (For interpretation of the references to color in this figure legend, the reader is referred to the Web version of this article.)

Table 2
Nominal chemical composition of the feedstock powder.

Element	Cr	Fe	Mo	Co	W	C	Ni
Content (%)	22	18	9	1.5	0.7	0.07	Balance

data processing and analysis were performed in a Matlab R2021b environment.

The MAX OT images were analyzed to detect spatter redeposits on the powder bed. As spatter redeposits manifest as bright blobs on OT images [11], the analysis procedure consists of blob detection, more specifically of convolution of the images with a Laplacian of Gaussian filter followed by non-minimum suppression, as described in previous work [11]. With that, the spatial coordinates of the spatter redeposits on OT images can be obtained. The oxygen content in the process atmosphere was monitored utilizing the oxygen sensor built-in EOS M290 (EOS GmbH).

2.3. Mechanical testing

Tensile tests were performed at room temperature using as-printed specimens, with geometry and dimensions as per Fig. 1c. The testing was done according to the ISO 6892-1 standard on an Instron 5582 universal electromechanical testing machine with a 100 kN load cell at a constant strain rate of $2{\cdot}10^{-3}$ s^{-1}.

The fatigue tests were performed at room temperature according to ISO 1099. The gauge and radius sections of the as-printed specimens represented in Fig. 1c were machined to remove 500 μm on all surfaces prior to fatigue testing, thus resulting in a gauge diameter of 6.0 mm. Before testing, grinding and polishing with SiC papers of decreasing grit size down to #4000 were performed on all samples. Fully-reversed ($R = -1$) stress-controlled fatigue tests with a frequency of 10 Hz were conducted at two stress ranges, 800 MPa and 900 MPa.

2.4. X-ray computed tomography

The gauge sections of machined specimens (Fig. 1c) were inspected on a custom-developed X-ray computed tomography (XCT) system prior to fatigue testing. The system consists of a microfocus X-ray tube (XWT-190-TCNF, X-RAY WorX), a 4000 × 4000 px^2 flat panel X-ray detector (XRD 1611 CP3, PerkinElmer), and air-bearing motion axes [27,28]. The X-ray tube was operated at a voltage of 180 kV and 15 W target power. A 1.0 mm copper filter was used to block low-energy X-rays and thus reduce beam hardening artifacts. In total, 4701 projections with an integration time of 4.0 s each and 2 × 2 pixel binning were recorded on a helical trajectory (848° scan angle, 12 mm pitch). Projection data were beam hardening corrected and reconstructed into a volume consisting of 2000 × 2000 × 6000 voxels with a voxel size of 4.36 μm using Siemens CERA 5.1.

XCT data analysis was performed in VG Studio MAX 3.4 (Volume Graphics). The volume data were filtered with a 3 × 3 × 3 median filter, and the outer sample surface was segmented using a gradient-based surface determination algorithm. Subsequently, a porosity analysis was performed using the VGEasyPore module with sub-voxel accuracy, a relative threshold of 50% and an area of 10 voxel to determine the local contrast. To render the analysis less prone to noise, defects were omitted if either the probability threshold (a non-disclosed quality metric) was below 0.1 %, the defect closer than 1 voxel to the outer sample surface, or the defect size below 8 voxel, representing an equivalent diameter of 0.011 mm. The positions of the detected defects relatively to each other and to the outer diameter of the specimen are accurately known, because the gauge section of the specimen was registered by least squares fitting a cylinder. However, their positions along the sample axis and angular positions are less accurate and estimated to be known to less than 0.1 mm and 2°, respectively. The z positions of the defects were, in all cases, centered using a cone fit on the beginning of the upper and lower tapered sections (radii). Their angular positions, relative to the engraving at the end of the sample end (sample label) were determined by the manual positioning of the specimen in the XCT scanner.

Some key defect characteristics obtained by XCT and analyzed in this work are defect size and sphericity. The defect size is defined as the diameter of the sphere circumscribed to the defect; the sphericity is defined as the ratio between the surface area of a sphere with the same volume as the defect and the surface area of the defect. The position of any given defect is given by the center of the sphere circumscribing the defect.

2.5. Fractography

After mechanical testing, fractographic analysis was performed in the specimens, firstly in a Zeiss Discovery V20 stereo optical microscope (SOM), then in a LEO Gemini 1550 scanning electron microscope (SEM). The fracture location (longitudinally to the specimen) was measured with a caliper in the adjacencies of the fracture initiation location. Considering the irregularity of the fracture surfaces, only the approximate z coordinate of the fracture initiation site was obtained.

2.6. Bulk chemical analysis

Bulk chemical analysis was performed by inert gas fusion using a LECO ON836 elemental analyzer at Höganäs AB to determine oxygen and nitrogen contents. The samples were pre-weighted, placed into a graphite crucible, and heated to release analyte gases, which were then detected by non-dispersive infrared (NDIR) cells.

2.7. Electron backscattered diffraction

The gauge sections of one machined specimen from each build job (in position 7A, as per Fig. 1) were analyzed using electron backscattered diffraction (EBSD). The gauge sections were sectioned both parallelly and perpendicularly to the building direction and mounted in a conductive resin. The samples were then prepared by plane grinding using 500 grit SiC paper, followed by fine grinding using a 9 μm diamond suspension. The polishing was done using 3 and 1 μm diamond suspensions. Final polishing was performed using a suspension of colloidal silica for a duration of 20 min. The EBSD maps were acquired in a Leo Gemini 1550 SEM equipped with a Nordlys II detector by Oxford Instruments. For the acquisitions an accelerating voltage of 20 kV was used and a step size between 7 and 3.5 μm was used. The data was analyzed using the MTEX toolbox [29].

3. Results and discussion

3.1. Microstructure, chemical composition and tensile behavior

Electron backscattered diffraction was performed in selected specimens from set 1 and set 2. EBSD orientation maps originating from the two sets are presented below in Fig. 2a. In both maps, the typical appearance of melt pools and elongated grains can be discerned. Grain areas were measured in larger corresponding maps, thus allowing the comparison of grain size distributions, presented in Fig. 2b. It is noticeable that set 2 displayed a shift in the distribution toward finer grains, which is expected based on the process parameters used during manufacturing: the melt pool dimensions are similar in both sets due to the constant laser parameters (energy distribution profile, spot size, power and scan speed) [30]; however, the larger nominal layer thickness in set 2 allows smaller volumes of material to be re-processed, thus restraining the epitaxial grain growth typically observed in additively manufactured materials [18].

Bulk chemical analysis was performed in chips extracted from tensile specimens at around 60 mm build height. For each set, the averages of two measurements are shown in Fig. 3a. The analysis revealed that

Fig. 2. (a) EBSD orientation maps along the build direction (BD) from the two sets. (b) Grain size distributions.

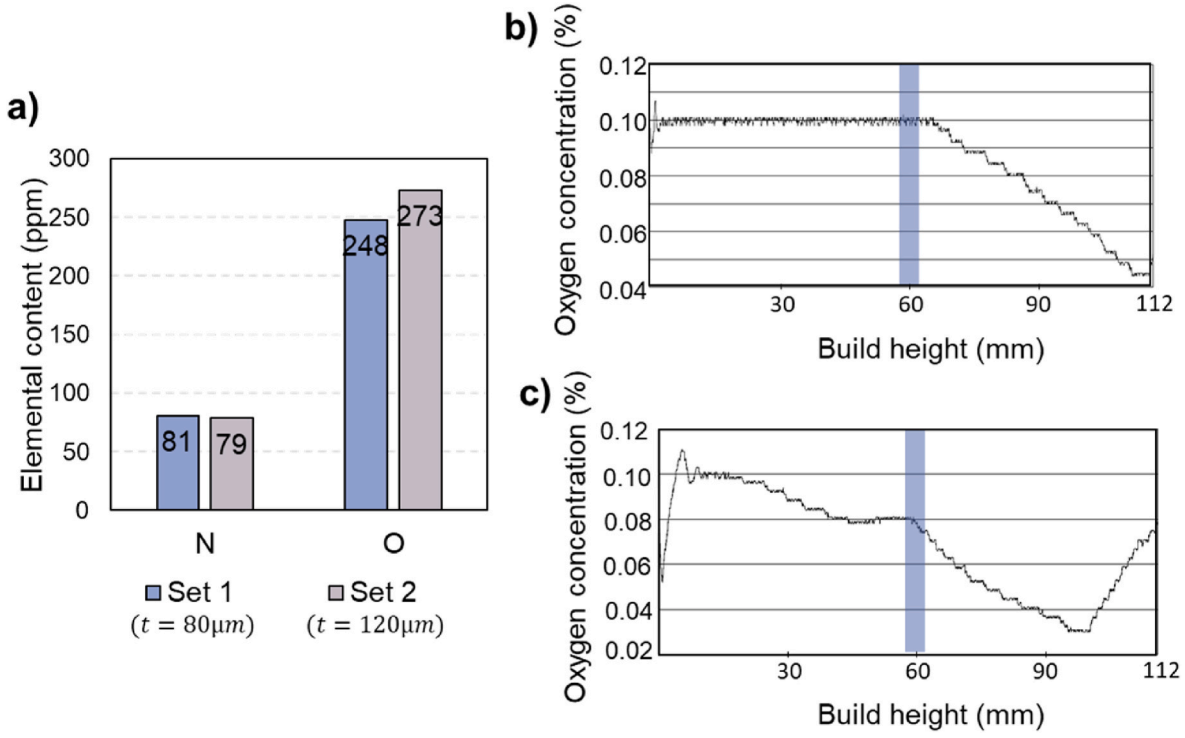

Fig. 3. (a) Bulk nitrogen and oxygen contents in samples of sets 1 and 2. Oxygen concentration in the build chamber during printing of specimens in set 1 (b) and set 2 (c). The sampling location is indicated in the plots (in blue). (For interpretation of the references to color in this figure legend, the reader is referred to the Web version of this article.)

specimens in set 2 contained 10% more oxygen, on average, than those in set 1, despite the slightly lower oxygen content in the build chamber in set 2, in the build height corresponding to the sampling locations, highlighted in Fig. 3b and c.

Previous studies have shown that the increase in nominal layer thickness prompts an increase in spatter formation in each layer [24] and susceptibility to lack of fusion [11,12] but an overall decrease in spatter formation for identical builds [31]. Fig. 5 indicates that increased nominal layer thickness provokes a slight increase in the bulk oxygen content, possibly due to the incorporation of spatter particles not involving fusion and release of oxygen to the same extent as for smaller nominal layer thicknesses.

Even though the focus of this study is evaluating the effect of spatter-induced defects on fatigue life, some tensile tests were performed for a better understanding of the mechanical properties of LPBF Hastelloy X. Three specimens from each set were tensile tested in the as-printed condition. The tested specimens were manufactured in positions 1C, 7C and 12C, as per Fig. 1B. The results are summarized in Fig. 4 and presented in Table 3 in the Appendix. Comparing the builds, the average yield strengths are identical, while slight variations were observed in the average tensile strength and elongation at fracture. Namely, the specimens built with higher productivity (set 2) presented an average 4% increase in tensile strength and an 8% decrease in elongation at fracture.

With a finer microstructure in set 2, higher yield and tensile strength would be expected, but only a slight difference in the latter was measured (Fig. 3). For LPBF-processed Hastelloy X, in addition to strengthening by solid solution and grain refinement, dislocation strengthening is active [32]. Since the dislocation strengthening in additively manufactured materials is chiefly dependent on the compression-tension cycles introduced by the layerwise melting [33], set 1, subjected to 50% more cycles, is more importantly affected by this mechanism. Thus, dislocation strengthening may provide additional

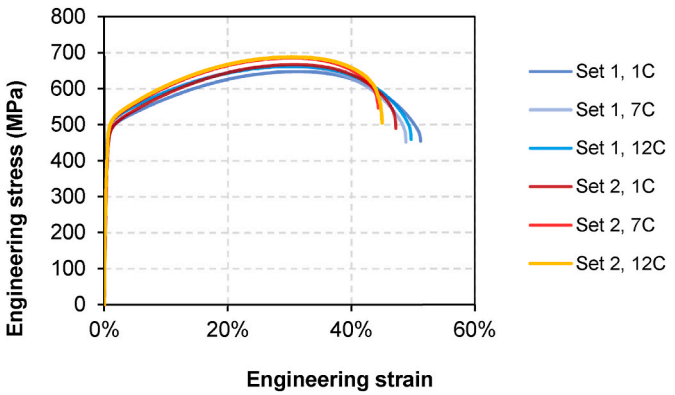

Fig. 4. Tensile test results for specimens manufactured in positions 1C, 7C and 12C from both sets of specimens.

resistance to yielding in set 1, compensating for the larger grain size. After yielding, dislocation strengthening becomes less active, while the grain size effect remains, thus explaining the difference in tensile strength.

Bulk oxygen content increase similar to the one measured this work (9%) has been reported to promote a slight increase in both tensile and yield strength [34] for Ti–6Al–4V, which was attributed to interstitial solid solution strengthening. As higher bulk oxygen content was measured in set 2, some minor effect of this strengthening mechanism could be expected. For LPBF Hastelloy X, as increase in oxygen content in the feedstock powder also resulted in slight increase in tensile and yield strength, but, more importantly, a significant reduction in the ductility [26], as observed in the present study. This difference was attributed, however, to the larger quantity of defects present in the material produced with recycled powder, richer in oxygen [26]. The presence of defects is investigated in the next subsection.

3.2. Detection of spatter redeposits via in-situ monitoring

One of the goals of this study is to evaluate the capability of the optical tomography in-situ monitoring to indicate materials quality and performance. Therefore, firstly the OT images acquired while printing the gauge section of the specimens were analyzed to detect spatter redeposits, which can form lack of fusion defects [9]. One OT image from each set is shown in Fig. 5a and c, together with their corresponding detections (in red). Considering the regions in the OT images corresponding to the gauge sections of the specimens, the total number of detections are 375 and 829 for in sets 1 and 2, respectively; thus, a larger number of defects is expected in set 2 [11,12], even though not all detections are expected to be associated with defects in the final part

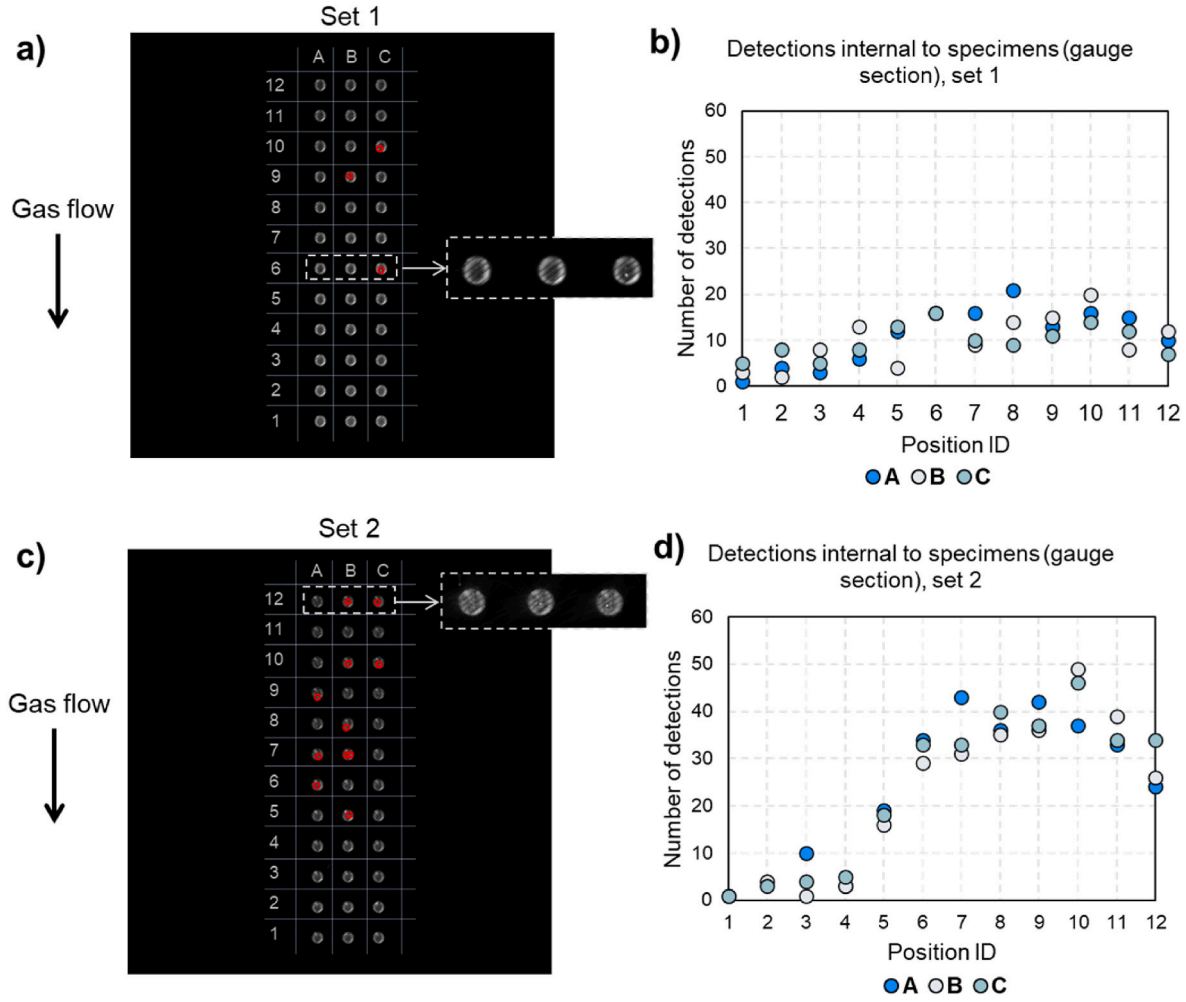

Fig. 5. Spatter redeposit detections in OT images during manufacturing of specimen sets 1 and 2. The superimposed grid indicates specimen identification. (a) and (c) show representative OT images overlayed with detections (in red) for sets 1 and 2, respectively. Portions of the original images are highlighted in the inserts. The number of detections internal to individual specimens in sets 1 and 2 is shown in (b) and (d), respectively. (For interpretation of the references to color in this figure legend, the reader is referred to the Web version of this article.)

[12]. This result agrees with the literature, as spattering is augmented with the use of larger nominal layer thicknesses [23], resulting in a larger quantity of spatters produced per layer [24]. With all laser parameters kept constant, the melt pool dimensions do not significantly vary between the sets of material [30]. However, the larger nominal layer thickness in set 2 implies that a smaller volume of material is remelted, which decreases the robustness to the disturbances introduced by redeposited spatter particles and thus increases the susceptibility to lack of fusion defects [12].

The defect populations of the tested tensile specimens can be estimated based on in-situ monitoring. Previous work has shown that multiple detections of spatter redeposits in OT images are often associated with a single spatter-induced LoF and that the number of detections tends to increase with the defect size [12]. Thus, defects located close to each other are highlighted in these plots (in red) to denote that they belong to a cluster and are more likely associated with a large defect. The decision criterion for proximity is the distance between detections less than or equal to 1.05 mm, which is the 80th percentile of the geometrical offset between the center of a defect and a detection [12].

The spatter redeposits detections made in the gauge section of the tensile specimens can be visualized in Fig. 6 as projections on the xz plane. The z-axis corresponds to the height within the gauge section, oriented along the build direction, and the x-axis is centered on the gauge section of each specimen and has the same orientation as the x-axis indicated in Fig. 1. The number of detections varies significantly among specimens, thus indicating variations in the defect populations, with specimens 7C and 12C in set 2 presumably containing considerable spatter-induced lack of fusion, according to Ref. [12].

The presumable more significant defect population present in specimens of set 2 may explain the tensile properties measured. While defects have a less significant effect under static loading [6], LoF defects have been found to be detrimental to tensile ductility [35]. Specifically, spatter-induced lack of fusion has been reported to be significantly detrimental to the ductility of additively manufactured materials [25,34]. A significant difference in the elongation to fracture was indeed observed in specimens of set 2 in relation to those is set 1, particularly for the specimens where abundant spatter redeposits were detected in OT images (7C and 12C).

3.3. Fatigue properties

The fully-reversed stress-controlled fatigue test results for Hastelloy X affected by spatter redeposition are presented in this section. The individual test results for sets 1 and 2 are also reported in Table 4 in the Appendix. The S–N curves for both sets of LPBF Hastelloy X specimens are seen in Fig. 7a. Superior overall performance is observed for the specimens in set 2, with average life around 50% higher than set 1 for both test stress ranges. However, the scatter in life is significantly larger for set 2 under the test stress range 800 MPa. In this test condition, the poorest performing specimens from each set have very similar lives (475k and 483k for sets 1 and 2, respectively), and the second poorest performer in set 2 had a life similar to the average in set 1. The best-performing specimen of set 2 had a 65% longer life than the best-performing in set 1. Considering that scatter in fatigue life of AM materials has been associated to the presence of defects [7,8], and that the analysis of in-situ monitoring data points towards a significantly higher defect content in set 2 (Fig. 5), the larger scatter observed in set 2 can tentatively be explained by the abundance of defects in this set. Further support to this claim is that fatigue failure is more sensitive to defects at lower stress ranges, where the elastic deformation is dominant [6], and where a more important scatter in fatigue life is observed (Fig. 7b). To confirm differences in defect populations between set 1 and set 2 and better understand the role of spatter-induced defects on the scatter of fatigue life, a screening of the defect populations in both sets of specimens is presented in subsection 3.3.1, based on XCT results. The XCT results are compared to the in-situ monitoring data of the corresponding specimens in subsection 3.3.2. Additionally, fractographic analysis is presented in subsection 3.3.3.

3.3.1. Defects measured via X-ray computed tomography

The gauge sections of several specimens of each set were measured via XCT post-machining and pre-testing. Fig. 8 shows the defect populations of these specimens, highlighting defect characteristics that differentiate pores from lack of fusion [12,36], namely their size and sphericity, which, combined, represent AM defects more realistically for analysis of fatigue performance [37]. The performance of these specimens is also presented for reference. Note that in set 1, five specimens were measured via XCT, but only four fatigue test results are presented. This is because the test of specimen 1B was deemed invalid due to interference of the extensometer, an issue mitigated in subsequent tests.

For set 1, only one of the examined specimens (11A) contained a defect that is presumably lack of fusion, i.e., a large defect with low sphericity. This observation points toward a higher robustness of the processing condition used [12], even though the specimens are not immune to spatter-induced defects. The scarcity of LoF in set 1 matches the low number of detections of spatter redeposits made in OT images, as shown in Fig. 5b. Specimen 11A, where a LoF of size 419 μm was identified via XCT, had a below-average performance in set 1 but outperformed another specimen where no LoF was identified (12B).

In set 2, only one of the specimens analyzed (1B) contained no

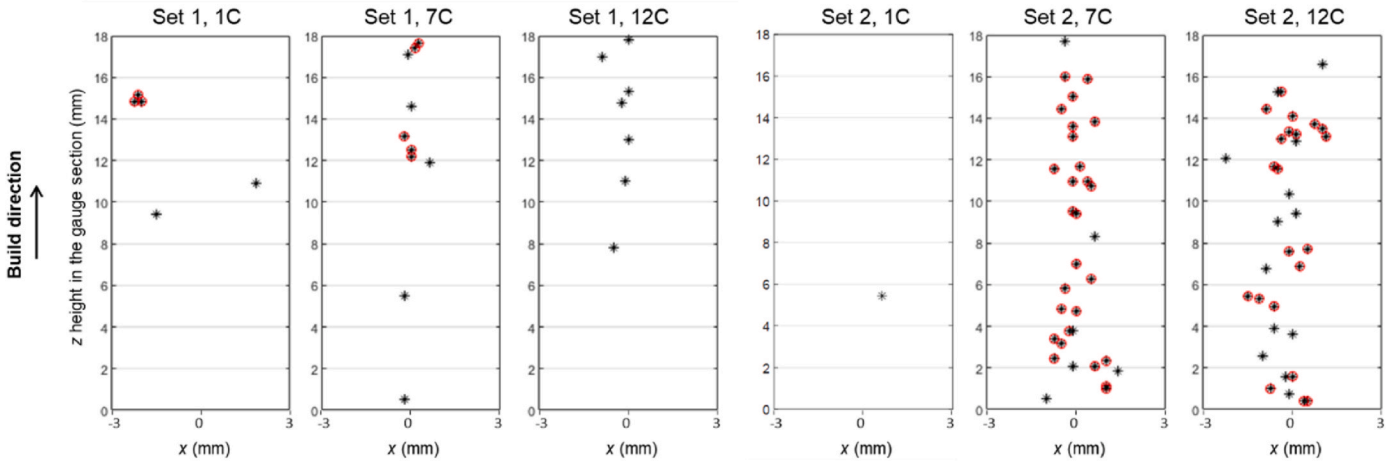

Fig. 6. Spatial representation of the OT spatter detections in the gauge sections of tensile specimens. Detections outlined in red belong to a cluster. (For interpretation of the references to color in this figure legend, the reader is referred to the Web version of this article.)

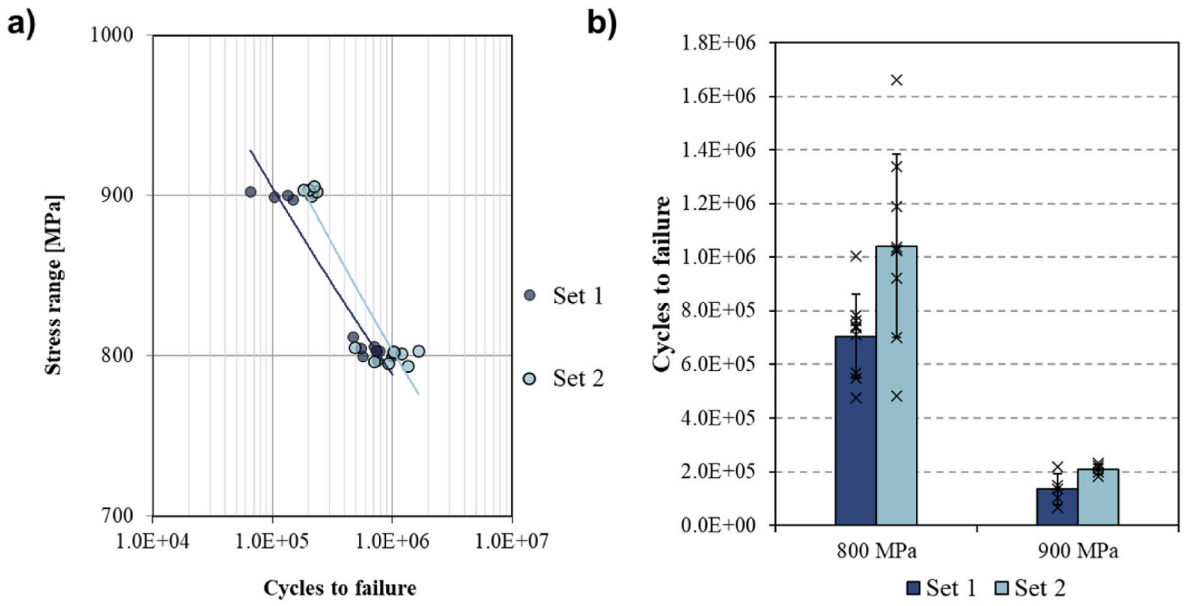

Fig. 7. Summary of fatigue properties. a) S–N curves for LPBF HX, sets 1 and 2. b) Average life of each set of specimens for the target stress ranges 800 MPa and 900 MPa. Individual data points are marked with a cross. The error bars represent one standard deviation from the average.

defects with characteristics of LoF. All remaining three specimens had multiple said defects, with the maximum defect size of 364 μm, 342 μm, and 401 μm for specimens 9A, 11A, and 12B, respectively. These results also match the predictions made via analysis of in-situ monitoring data, where abundant spatter redeposits were detected in specimens located upstream on of the build area (i.e. positions 6–12, as seen in Fig. 5). Despite the major differences in defect populations, the four specimens presented a comparable fatigue performance, within plus or minus one standard deviation from the average life in the group. Interestingly, all four specimens in set 2 outperformed the four specimens in set 1, despite the minor defect content of the latter, and identical specimen geometries and testing conditions used.

3.3.2. *Correspondence between spatter detections and internal defects*

The spatial distribution of the LoF defects identified in the gauge section of the specimens via XCT are represented in Fig. 9, where the defect centers are plotted. The corresponding spatial distributions of OT detections are shown besides the XCT data. The *z* axis is aligned with the build direction. In Fig. 9 (a, c, e, g), it is noticeable that lack of fusion defects are present across extensive ranges of the analyzed area. The approximate final fracture location, represented in the images as a dashed line, hints that the fatigue failure is not associated with LoF in at least two cases (specimen 11A set 1, and 9A set 2), as no LoF are present in the failure region. In the remaining two specimens, LoF could be present in the fatigue fracture region, considering that the errors in the measurement of the fracture locations do not allow categorical statements.

The spatter detections in OT images of the corresponding gauge sections can be seen in Fig. 9 (b, d, f, h). For specimen 11A, set 1, 15 detections are present, three of which compose a cluster at the *z*-height (in the gauge section) of approximately 9 mm (Fig. 9b), which corresponds to the approximate *z* coordinate of the single lack of fusion identified in this specimen (Fig. 9a). In specimen 9A set 2, many clustered spatter detections and LoF are present across the gauge section, except between the heights of 4 and 8 mm approximately. Despite that, the fracture occurred in this region, as represented by the red dotted line in Fig. 9c and d. In specimen 12B set 2, clusters of detections are present up to *z* height of approximately 5 mm (Fig. 9h). The XCT data reveals that this region is particularly dense in LoF, containing multiple defects larger than 250 μm (Fig. 9g). The fracture location was measured at a z-height of approximately 12.8 mm, where a couple of spatter detections and defects are present, one larger than 250 μm.

Thus, the XCT and OT results reveal that the phenomenon investigated in this study, spatter-induced defect formation, is present in the specimens, and that extent and location of spatter redeposits, particularly when in clusters, match the LoF measured in XCT. However, the combined analysis of XCT and fatigue test results indicate that these defects do not necessarily promote a significant underperformance of the material, even though it might influence the scatter in properties within a group. The fracture location measurements show that the fracture may occur in a LoF-free region, despite multiple LoF elsewhere in the gauge section. To determine whether and to what extent this is the case, the fracture surfaces of all specimens are examined in the next subsection.

3.3.3. *Fractography*

The fracture surfaces of the fatigue specimens in set 1 are depicted in Fig. 10, where the crack initiation sites are also indicated and categorized. Almost all specimens tested at the 800 MPa stress range had an internal crack initiation site. Only specimens 11A and 12B, with the poorest performances in this subgroup, presented surface initiation. Analysis of the fracture surfaces revealed that the internal initiation sites are material discontinuities other than defects, e.g., grain boundaries, melt pool boundaries and their combination. None of the specimens in set 1 presented LoF defects on the fracture surfaces, which could be expected based on the low number of said defects expected from the XCT screening (Fig. 8) and from analysis of OT data (Figs. 5 and 14 in the appendix, which shows the spatial distribution of the OT spatter detections).

On the other hand, a high number of LoF defects were identified in set 2, apart from the more significant scatter in fatigue data that could be due to defects. The fracture surfaces of the fatigue specimens in set 2 are depicted in Fig. 11, together with the categorized crack initiation sites. Seven of the nine specimens tested at the 800 MPa stress range had internal crack initiation sites, but in only three of them (9A, 11A, 12B) LoF defects were identified in the initiation sites. These specimens had varying performances within the group, as noticeable in Fig. 11. Thus, the presence of LoF as fatigue crack initiator appears not to necessarily be correlated to a poorer fatigue performance of this material. Indeed, the specimens that presented the poorest performance in this subgroup

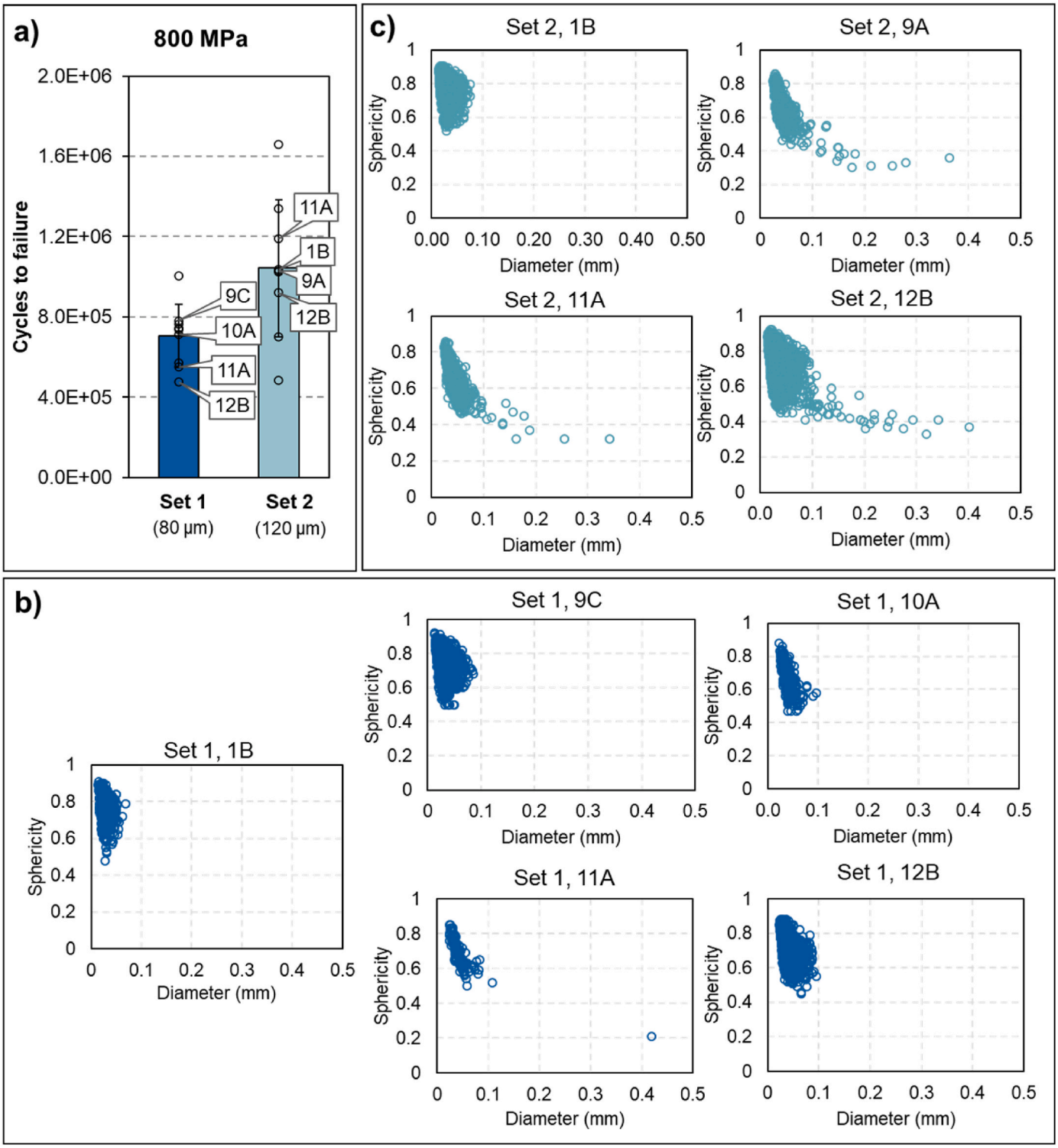

Fig. 8. Internal defects identified via XCT in the gauge sections of nine fatigue specimens. a) Fatigue performance of the measured specimens highlighted in their groups. The target test stress range is indicated. Defect size vs. defect sphericity for specimens in sets 1 (b) and 2 (c).

(5B and 11B) presented fatigue crack initiation site at the surface. Common to sets 1 and 2, all specimens tested at 900 MPa stress range had surface initiating fracture. This observation is in accordance with the literature, as cracks tend to initiate from internal features in high cycle fatigue and from the surface at shorter fatigue life [6].

The fracture surface of one of these poor-performing specimens, 11B set 2 is shown in further detail in Fig. 12, where no LoF defects are visible. In the SOM image presented for reference (Fig. 12d), radial marks are visible, pointing towards the origin, indicated by an arrow. The shear lip can be seen on the opposing side of the fracture surface. The remaining images were taken in the SEM. Fig. 12e is a low magnification image in which the regions magnified in (a)-(c) and (f) are outlined by rectangles. The region nearest the crack initiation (f) has a faceted aspect. No defects were observed on the initiation site. Striations are visible in (b) and (c), in which the direction of crack propagation is indicated. Fig. 12a represents the region of the fracture surface where

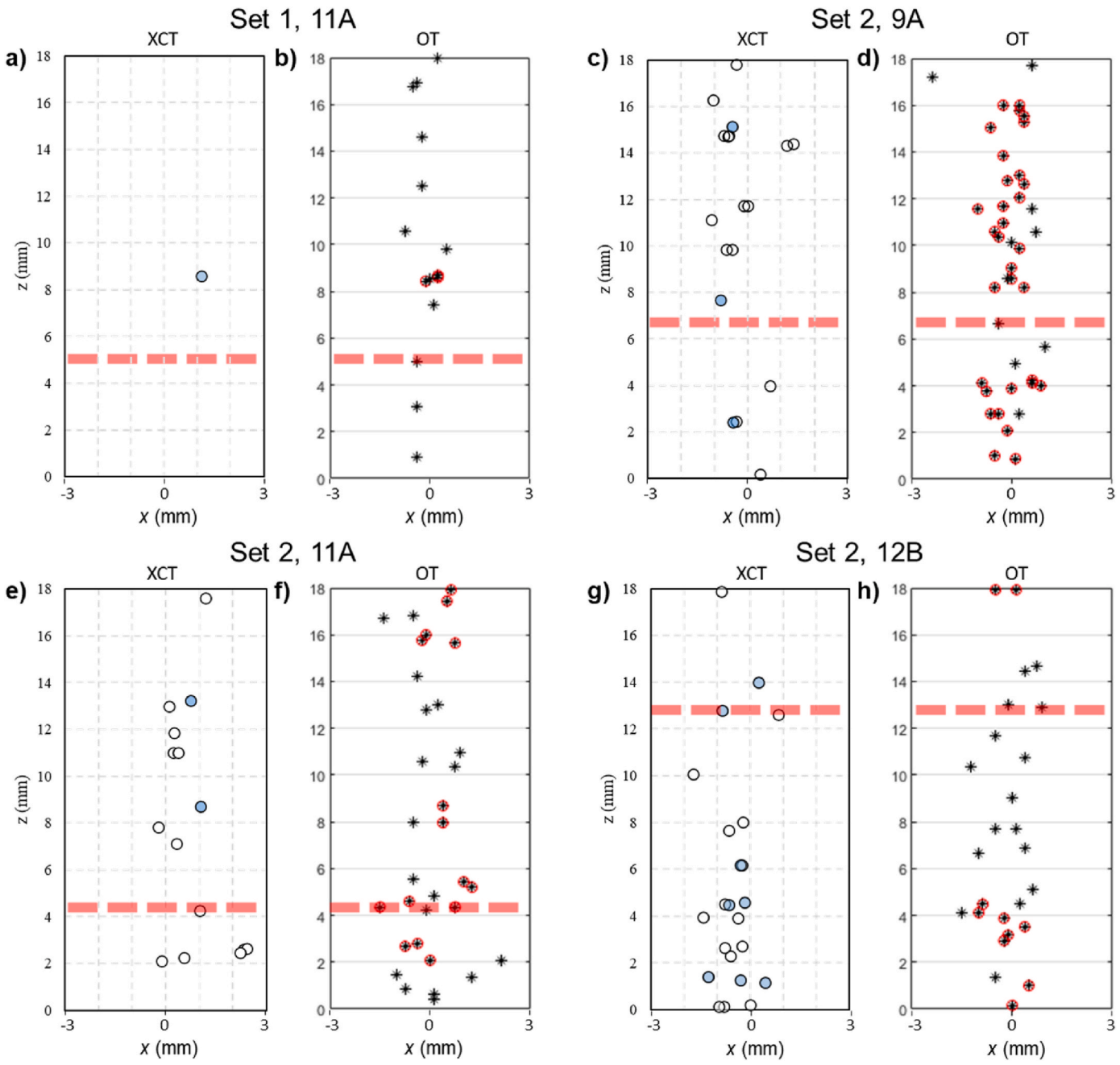

Fig. 9. Positions of LoF defects (centers) identified via XCT for the four measured specimens in which LoF were identified are represented in (a), (c), (e), (g). Defects of size 250 μm or larger are indicated in blue. The corresponding spatter redeposit detections made in OT images are seen in (b), (d), (f), and (h). Detections outlined in red belong to a cluster. The dotted lines represent the fracture locations. (For interpretation of the references to color in this figure legend, the reader is referred to the Web version of this article.)

the final fracture happened and presents a ductile aspect.

In contrast, to showcase a specimen where LoF defects played an important role in fatigue fracture, detailed images of the fracture surface of specimen 12B set 2 can be seen in Fig. 13. In this specimens, clusters of detections were present in this specimen's OT data, but nowhere close to the fracture location, where individual detections were made instead (Fig. 9h). The SOM analysis indicated potential defects as the crack initiation sites, which was confirmed by SEM analysis. Three LoF were identified (Fig. 13b), two smaller ones near each other (Fig. 13c) and one larger defect of size ~260 μm (Fig. 13e). Note that a LoF in this size range was identified via XCT in the build height corresponding to the fracture location (Fig. 9g). Also, two spatter detections were made in OT images of consecutive layers in this location (Fig. 9h). In the largest LoF defects on the fracture surface, unfused particles and possibly oxide patches are visible (Fig. 13e). In addition, a spherical depression of size ~55 μm is visible in the immediate vicinity of one of the LoF (Fig. 13f). Despite multiple large lack of fusion defects, the specimen presented fair fatigue performance, albeit in the lower range of its group. From the XCT defects data in Fig. 8c, it is noticeable that larger defects exist in the gauge section of this sample; however, they did not act as crack initiators. The same was observed for the remaining specimens containing multiple LoF confirmed by XCT (9A and 11A in set 2, Fig. 9): despite their abundant LoF, some even clustered in the bulk, and crack initiation sites at LoF defects (Fig. 11), their performance was comparable to specimen 1B, containing no lack of fusion according to XCT data (Fig. 8), and no spatter redeposits detected in OT images (Fig. 15 in the

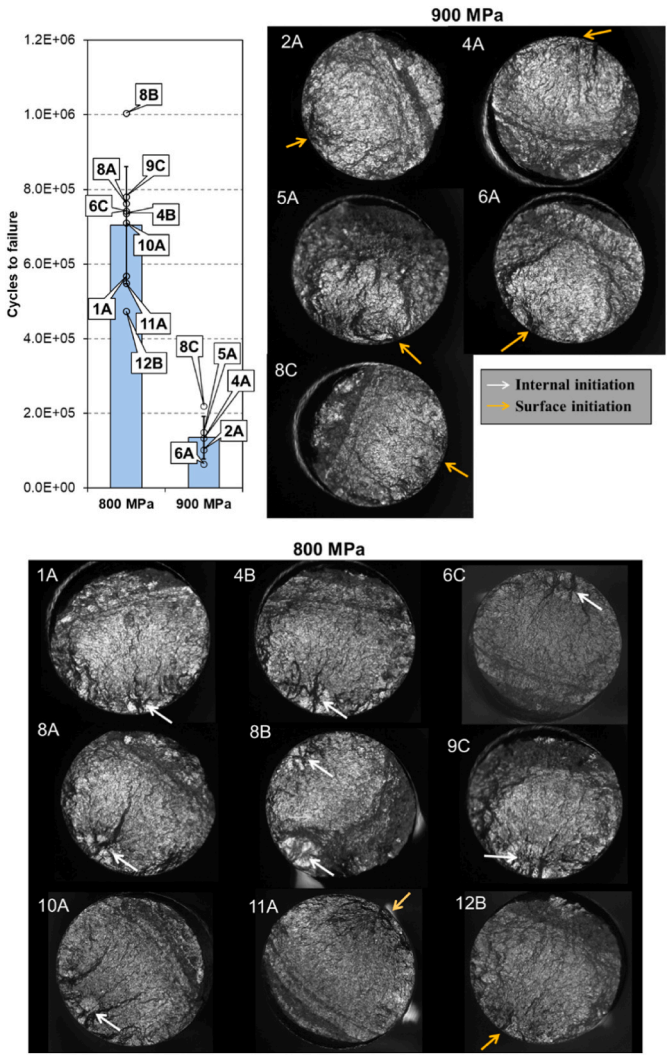

Fig. 10. Fracture surfaces of fatigue specimens in set 1. The target stress ranges are indicated. The crack initiation sites are color-coded according to the type of initiation. The performance of each specimen is shown for reference. (For interpretation of the references to color in this figure legend, the reader is referred to the Web version of this article.)

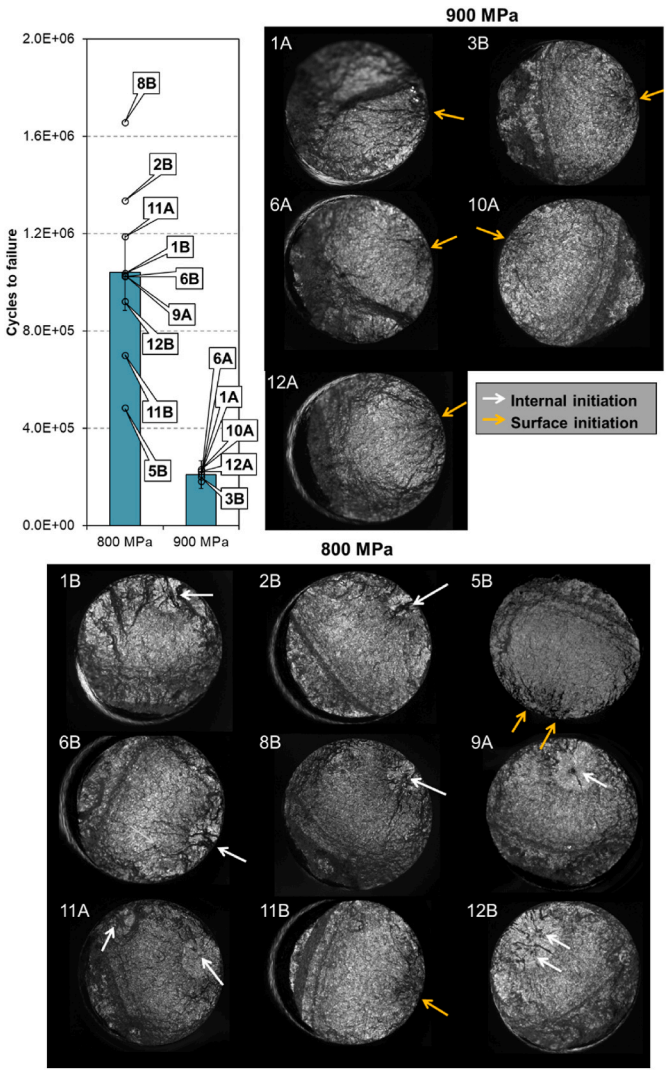

Fig. 11. Fracture surfaces of fatigue specimens in set 2. The target stress ranges are indicated. The crack initiation sites are color-coded according to the type of initiation. The performance of each specimen is shown for reference. (For interpretation of the references to color in this figure legend, the reader is referred to the Web version of this article.)

appendix).

The results indicate that spatter-induced lack of fusion defects have only a limited influence on the fatigue performance of Hastelloy X as: a) several specimens containing numerous large LoF outperform LoF-free specimens, both within sets of material and across sets; b) specimens containing numerous large LoF fracture in LoF-free regions; c) the specimens with the shortest fatigue lives did not contain defects on the fracture surface. These points are discussed next.

Regarding specimens in set 2 (with abundant LoF) outperforming specimens in set 1 (predominantly LoF-free), similar observations have previously been made when comparing two sets of LPBF Ti–6Al–4V specimens, where one of the sets contained multiple lack of fusion but still outperformed the set that did not present such defects [38]. This surprising result was attributed to differences in microstructure and chemistry. In the present study, a striking difference in the microstructure is indeed observed in between sets, with set 2 having a finer microstructure. It is widely reported that finer microstructures benefit fatigue performance, as demonstrated for several AM alloys [39,40], including Hastelloy X [41]. Materials with finer microstructures have more resistance to crack initiation by impeding dislocation motion, which also has a strengthening effect [6], and propagation, for entailing a more tortuous crack propagation route [42]. As the difference in microstructure is systemic within a set, it can explain the approximately 50% higher average fatigue life of set 2. Interestingly, set 2 outperformed set 1 equally in both test stress ranges, when distinct factors control fatigue performance at short and long lives. At short lives, ductility controls performance, as plastic strain predominates, while at longer lives, strength is the controlling factor, since elastic strain predominates [43]. While only slight differences in strength were identified between the sets, an average 8% ductility reduction was measured for set 2. Nonetheless, set 2 performed better on average even at short lives, indicating a dominant effect of its finer microstructure.

It was also observed that specimens with numerous large LoF could outperform LoF-free specimens within the same group, i.e., manufactured with identical processing conditions and presenting the same microstructure. This further indicates LPBF Hastelloy X has a low sensitivity to internal defects. Sensitivity to defects is typically associated with the material's ductility, as high ductility reduces notch sensitivity [43,44]. Even though some difference in ductility was found between sets, all elongation at fracture measurements are above 40%, meaning that the material has a high ductility and indicating its overall robustness to the effect of defects on fatigue performance.

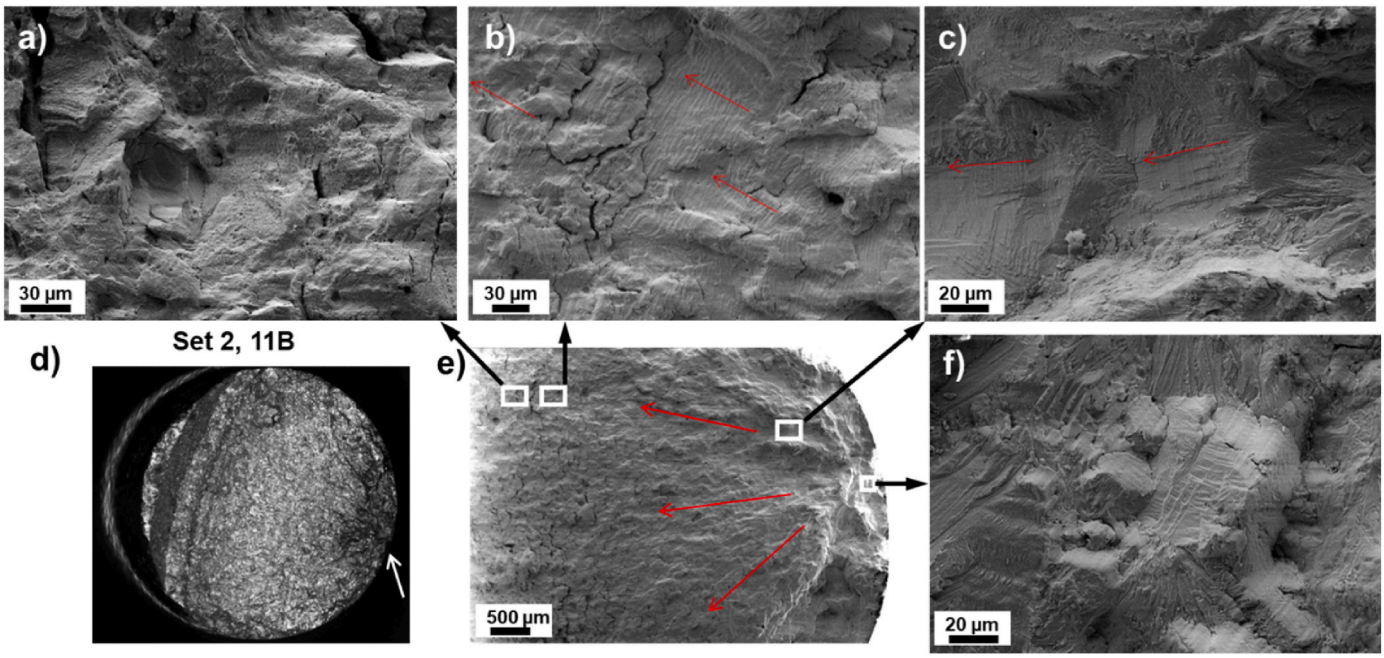

Fig. 12. Fracture surface of specimen 11B, set 2. A SOM image (d) and a low-magnification SEM image (e) are presented for reference. In (e), the regions magnified in (a)–(c) and (f) are outlined by rectangles. A region near the crack initiation, stage I of the fracture, is shown in (f). Stage II is depicted in (b) and (c). Stage III is depicted in (a). The direction of crack propagation is indicated with red arrows. (For interpretation of the references to color in this figure legend, the reader is referred to the Web version of this article.)

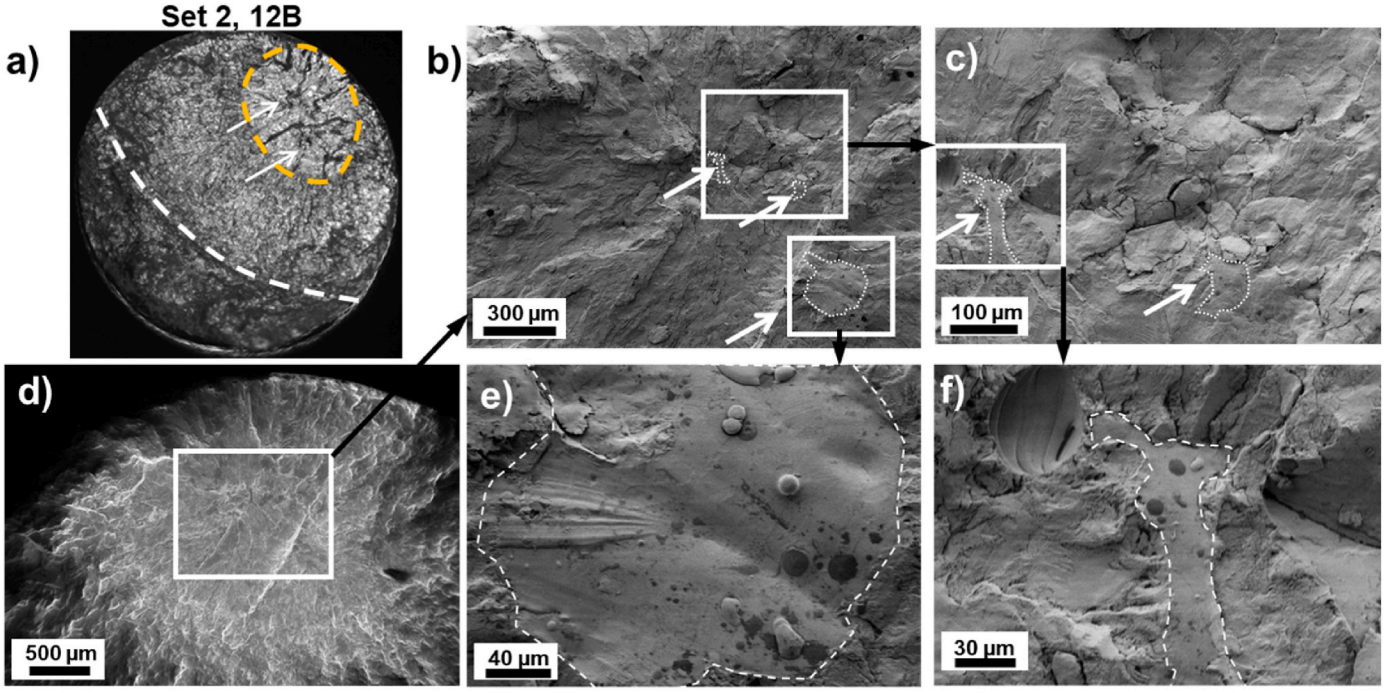

Fig. 13. Fracture surface of specimen 12B, set 2, highlighting the crack initiation region. Lack of fusion defects, identified as the initiation sites, are indicated by white arrows and outlined. The images were acquired with SOM (a) and SEM (b–f).

Regarding the second and third points, specimens containing numerous large LoF might fracture elsewhere because other microstructural features can dominate fatigue failure [42]. In a study of the fatigue life of LPBF 316L, also a material with high ductility and low sensitivity to defects, most fatigue crack initiation took place in slip planes in dendrite cells and grain boundary particles [43]. Since the location of the potential initiation feature is key [13], with near-surface being more important, the occurrence of these critical microstructural features near-surface might dominate, dropping the lives of the specimens where this occurs. This appears to be the case for the low-range outliers in both sets, that presented surface initiation and no LoF on the fracture surface. Lastly, initiating defects have been found to not be amongst the largest defects within the gauge section of a specimen, which can also be explained by other factors than defect size (e.g., defect

location and orientation) playing a role in crack initiation. Similar observations have been made in the study of the fatigue performance of AM titanium alloys, in which the initiating defects were not the largest but in the top 35% [8].

The largest defects observed in this study do not exceed 500 μm, and can be regarded as moderately sized, considering that abundant spatter-induced LoF larger than 1 mm and up to 4 mm has been observed in previous work [12]. The oversized LoF were present predominantly in the material manufactured with nominal layer thicknesses larger than the ones used in the present study. Thus, the relatively low significance of defects in the size range found for $t = 120\ \mu m$ might enable the use of processing conditions with higher productivity for further application areas.

4. Conclusions

This study investigated how increased productivity influences spatter-driven defect formation and mechanical properties of as-printed Hastelloy X at room temperature, with focus on fatigue performance. Test specimens were manufactured with nominal layer thicknesses of 80 μm and 120 μm. Spatter redeposits were detected in optical tomography images acquired in-situ, whereby the presence of defects could be inferred. A few specimens were measured via X-ray computed tomography, confirming the presence of defects. The specimens were mechanically tested, and their performance was correlated to their defect populations. The results can be summarized as follows.

Hastelloy X manufactured with higher productivity (set 2) contained more significant spatter-induced lack of fusion, which introduced variability in the ductility. On the other hand, it presented finer microstructure, and higher oxygen content, both factors that should be beneficial to the tensile strength. However, the increased thermal cycles of the Hastelloy X produced with thinner powder layers (lower productivity) likely rendered it more significantly strengthened by dislocation strengthening, thus compensating the grain refinement and solid solution strengthening in set 2 and rendering materials with similar strengths. Despite being more affected by spatter redeposition and demonstrably containing spatter-induced lack of fusion, the specimens manufactured at a higher build rate (set 2) presented superior average fatigue properties, indicating a dominant effect of its finer microstructure.

While lack of fusion defects could be induced by spatter redeposition, as verified by XCT and predicted by analysis of monitoring data, they had limited influence on the fatigue performance of Hastelloy X. This is attributed to the low sensitivity of this alloy to defects, corroborated by its high ductility, the moderate size of the lack of fusion defects, and the more important influence of the microstructure in the fatigue performance.

In case the fatigue design for an application primarily considers the scatter in life, a clear benefit exists from using OT monitoring, as it indicates the formation of spatter-induced lack of fusion. This type of defect has been associated with a higher spread in life within a group, even though individual large defects do not necessarily yield poor fatigue performance. The effect of microstructure refinement appears to override the impact of large spatter-induced lack of fusion defects in the fatigue life of ductile materials such as LPBF Hastelloy X.

Declaration of competing interest

The authors declare that they have no known competing financial interests or personal relationships that could have appeared to influence the work reported in this paper.

Acknowledgments

This work was conducted within the framework of the project MANUELA - Additive Manufacturing using Metal Pilot Line, funded by European Union's Horizon 2020 research and innovation programme under grant agreement no. 820774. The authors acknowledge project DYNAMIQ and the Centre for Additive Manufacturing – Metal (CAM2), both supported by the Swedish Governmental Agency of Innovation Systems (Vinnova), and the Production Area of Advance, Chalmers University of Technology. The authors acknowledge Höganäs AB for the support with chemical analysis.

Appendix

Table 3
Tensile test results from sets 1 and 2.

Specimen	Ultimate tensile strength (MPa)	Yield strength (MPa)	Elongation at fracture (%)
Set 1, 1C	648	468	51
Set 1, 7C	662	477	49
Set 1, 12C	662	492	50
Set 2, 1C	667	464	47
Set 2, 7C	686	485	44
Set 2, 12C	688	489	45

Table 4
Fatigue test results from sets 1 and 2

Batch	Specimen ID	Number of cycles	Stress range (MPa)
Set 1	1A	569,679	800
Set 1	2A	103,676	899
Set 1	4A	135,540	900
Set 1	4B	736,638	803
Set 1	5A	150,094	898
Set 1	6A	65,929	902
Set 1	6C	743,225	803
Set 1	8A	763,402	797
Set 1	8B	1,005,429	800
Set 1	8C	219,991	901

(*continued on next page*)

Table 4 (*continued*)

Batch	Specimen ID	Number of cycles	Stress range (MPa)
Set 1	9C	781,622	803
Set 1	10A	711,968	805
Set 1	11A	550,146	804
Set 1	12B	474,784	812
Set 2	1A	211,869	900
Set 2	1B	1,037,144	802
Set 2	2B	1,338,522	794
Set 2	3B	199,186	904
Set 2	5B	483,472	806
Set 2	6A	182,458	904
Set 2	6B	1,022,908	803
Set 2	8B	1,660,316	803
Set 2	9A	1,027,384	802
Set 2	10A	232,066	903
Set 2	11A	1,189,190	801
Set 2	11B	700,026	796
Set 2	12A	222,453	906
Set 2	12B	921,071	796

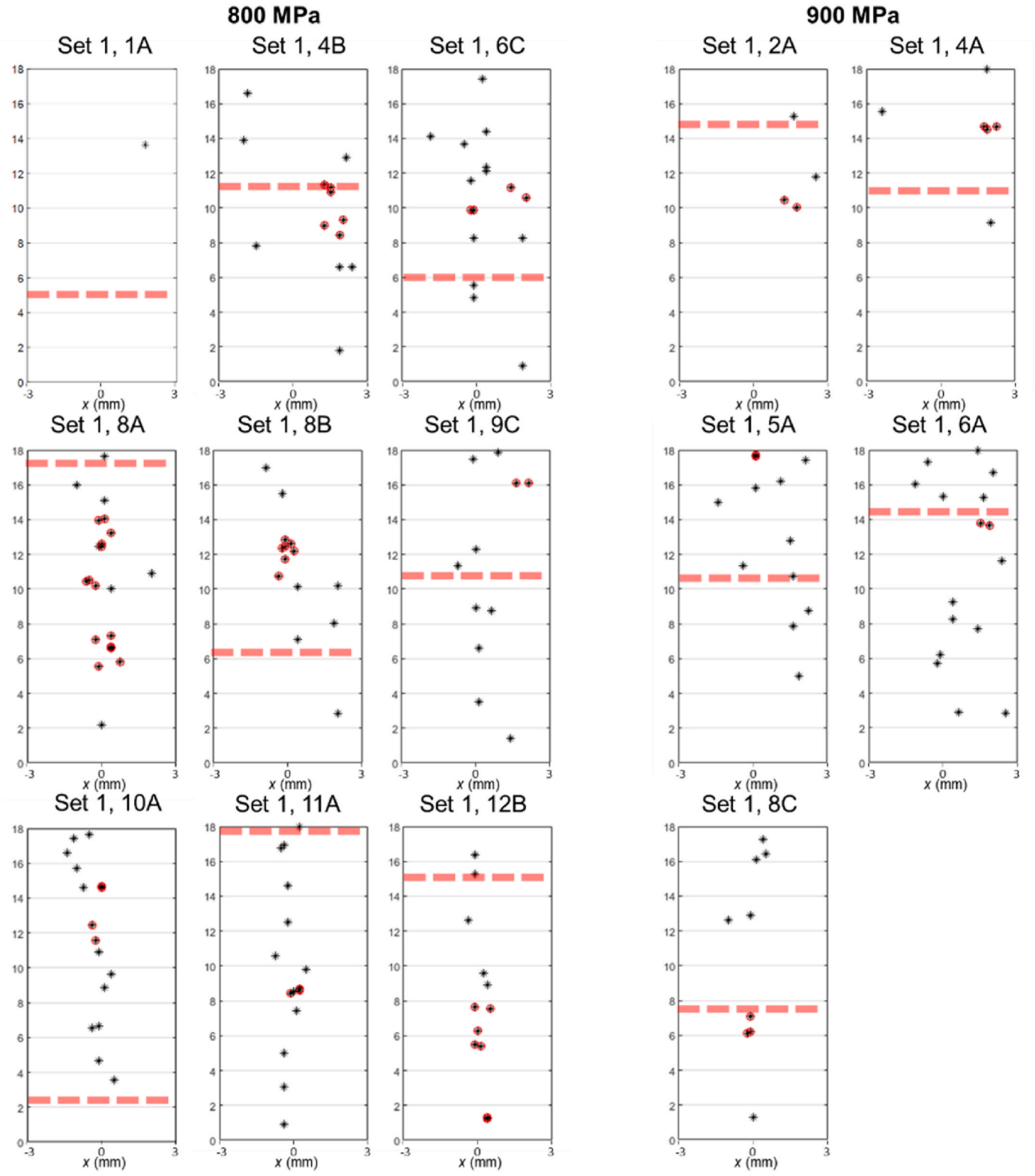

Fig. 14. Spatial representation of the OT spatter detections in the gauge sections of the specimens in set 1. Detections outlined in red belong to a cluster. The dotted lines represent the fracture locations.

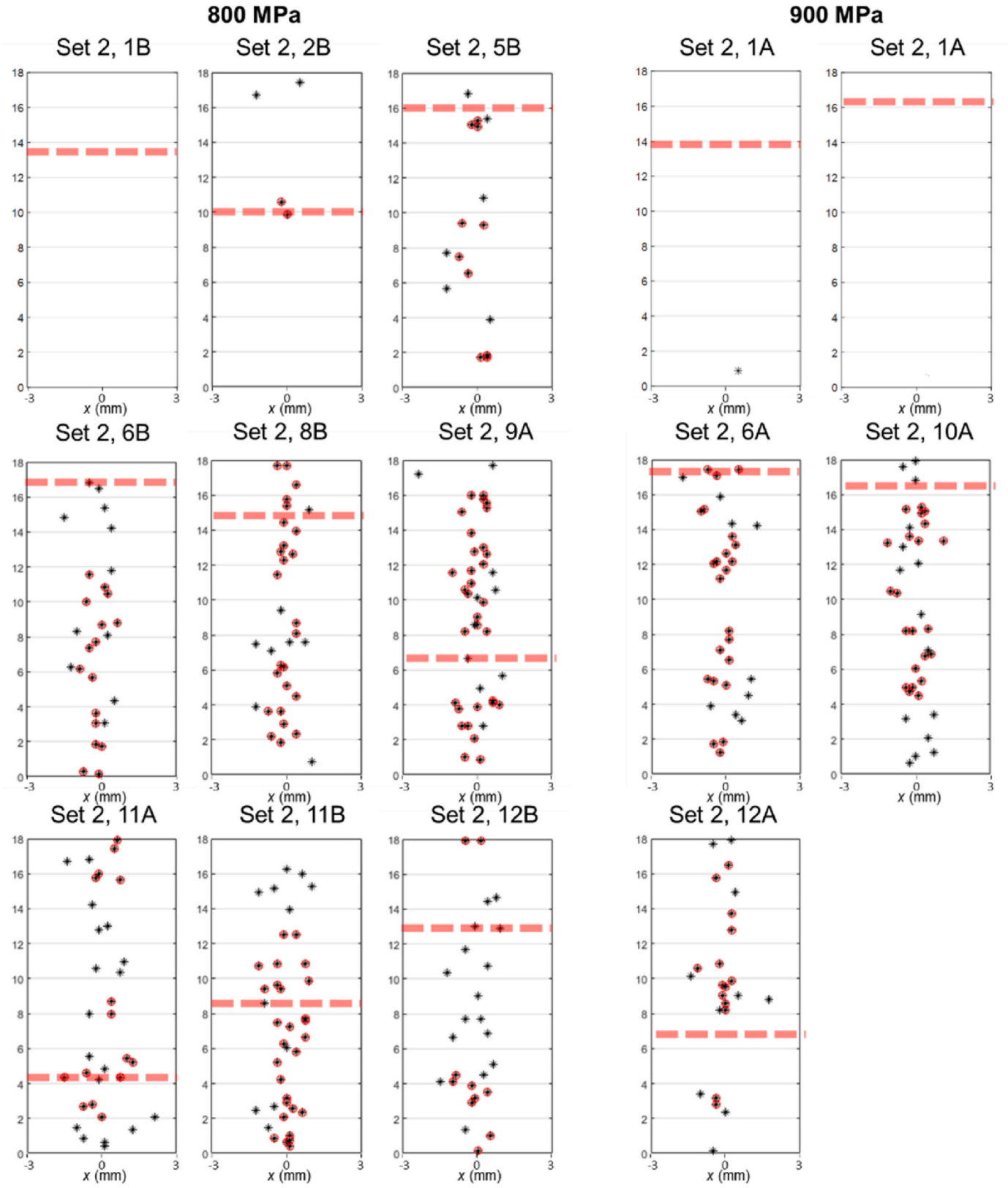

Fig. 15. Spatial representation of the OT spatter detections in the gauge sections of the specimens in set 2. Detections outlined in red belong to a cluster. The dotted lines represent the fracture locations.

References

[1] de Formanoir C, Paggi U, Colebrants T, Thijs L, Li G, Vanmeensel K, Van Hooreweder B. Increasing the productivity of laser powder bed fusion: influence of the hull-bulk strategy on part quality, microstructure and mechanical performance of Ti-6Al-4V. Addit Manuf 2020;33. https://doi.org/10.1016/j.addma.2020.101129.

[2] Taghian M, Mosallanejad MH, Lannunziata E, Del Greco G, Iuliano L, Saboori A. Laser powder bed fusion of metallic components: Latest progress in productivity, quality, and cost perspectives. J Mater Res Technol 2023;27:6484–500. https://doi.org/10.1016/j.jmrt.2023.11.049.

[3] Venturi F, Taylor R. Additive manufacturing in the Context of repeatability and reliability. https://doi.org/10.1007/s11665-023-07897-3; 2023.

[4] Wu Z, Wu S, Qian W, Zhang H, Zhu H, Chen Q, Zhang Z, Guo F, Wang J, Withers PJ. Structural integrity issues of additively manufactured railway components: progress and challenges. Eng Fail Anal 2023;149:107265. https://doi.org/10.1016/j.engfailanal.2023.107265.

[5] Mostafaei A, Zhao C, He Y, Reza Ghiaasiaan S, Shi B, Shao S, Shamsaei N, Wu Z, Kouraytem N, Sun T, Pauza J, Gordon JV, Webler B, Parab ND, Asherloo M, Guo Q, Chen L, Rollett AD. Defects and anomalies in powder bed fusion metal additive manufacturing. Curr Opin Solid State Mater Sci 2022;26:100974. https://doi.org/10.1016/j.cossms.2021.100974.

[6] Sanaei N, Fatemi A. Progress in Materials Science Defects in additive manufactured metals and their effect on fatigue performance : a state-of-the-art review. Prog Mater Sci 2021;117:100724. https://doi.org/10.1016/j.pmatsci.2020.100724.

[7] Romano S, Brückner-Foit A, Brandão A, Gumpinger J, Ghidini T, Beretta S. Fatigue properties of AlSi10Mg obtained by additive manufacturing: defect-based modelling and prediction of fatigue strength. Eng Fract Mech 2018;187:165–89. https://doi.org/10.1016/J.ENGFRACMECH.2017.11.002.

[8] Tammas-Williams S, Withers PJ, Todd I, Prangnell PB. The influence of porosity on fatigue crack initiation in additively manufactured titanium components. Sci. Reports 2017 2017;71(7):1–13. https://doi.org/10.1038/s41598-017-06504-5.

[9] Ladewig A, Schlick G, Fisser M, Schulze V, Glatzel U. Influence of the shielding gas flow on the removal of process by-products in the selective laser melting process. Addit Manuf 2016;10:1–9. https://doi.org/10.1016/j.addma.2016.01.004.

[10] Delacroix T, Lomello F, Schuster F, Maskrot H, Garandet JP. Influence of powder recycling on 316L stainless steel feedstocks and printed parts in laser powder bed fusion. Addit Manuf 2022;50:102553. https://doi.org/10.1016/J.ADDMA.2021.102553.

[11] Schwerz C, Raza A, Lei X, Nyborg L, Hryha E, Wirdelius H. In-situ detection of redeposited spatter and its influence on the formation of internal flaws in laser powder bed fusion. Addit Manuf 2021:102370. https://doi.org/10.1016/J.ADDMA.2021.102370.

[12] Schwerz C, Bircher BA, Küng A, Nyborg L. In-situ detection of stochastic spatter-driven lack of fusion: application of optical tomography and validation via ex-situ X-ray computed tomography. Addit Manuf 2023:103631. https://doi.org/10.1016/J.ADDMA.2023.103631.

[13] Beretta S, Romano S. A comparison of fatigue strength sensitivity to defects for materials manufactured by AM or traditional processes. Int J Fatig 2017;94:178–91. https://doi.org/10.1016/j.ijfatigue.2016.06.020.

[14] Wong H, Dawson K, Ravi GA, Howlett L, Jones RO, Sutcliffe CJ. Multi-laser powder bed fusion benchmarking—initial trials with inconel 625. Int J Adv Manuf Technol 2019;105:2891–906. https://doi.org/10.1007/S00170-019-04417-3/FIGURES/14.

[15] Schleifenbaum H, Diatlov A, Hinke C, Bültmann J, Voswinckel H. Direct photonic production: towards high speed additive manufacturing of individualized goods. Prod Eng 2011;5:359–71. https://doi.org/10.1007/s11740-011-0331-0.

[16] Ma M, Wang Z, Gao M, Zeng X. Layer thickness dependence of performance in high-power selective laser melting of 1Cr18Ni9Ti stainless steel. J Mater Process Technol 2015;215:142–50. https://doi.org/10.1016/j.jmatprotec.2014.07.034.

[17] Sun Z, Tan X, Tor SB, Yeong WY. Selective laser melting of stainless steel 316L with low porosity and high build rates. Mater Des 2016. https://doi.org/10.1016/j.matdes.2016.05.035.

[18] Schwerz C, Schulz F, Natesan E, Nyborg L. Increasing productivity of laser powder bed fusion manufactured Hastelloy X through modification of process parameters. J Manuf Process 2022;78:231–41. https://doi.org/10.1016/J.JMAPRO.2022.04.013.

[19] Cutolo A, Neirinck B, Lietaert K, de Formanoir C, Van Hooreweder B. Influence of layer thickness and post-process treatments on the fatigue properties of CoCr scaffolds produced by laser powder bed fusion. Addit Manuf 2018;23:498–504. https://doi.org/10.1016/j.addma.2018.07.008.

[20] Taheri Andani M, Dehghani R, Karamooz-Ravari MR, Mirzaeifar R, Ni J. Spatter formation in selective laser melting process using multi-laser technology. Mater Des 2017;131:460–9. https://doi.org/10.1016/j.matdes.2017.06.040.

[21] Liu Y, Yang Y, Mai S, Wang D, Song C. Investigation into spatter behavior during selective laser melting of AISI 316L stainless steel powder. Mater Des 2015;87:797–806. https://doi.org/10.1016/j.matdes.2015.08.086.

[22] Wang D, Wu S, Fu F, Mai S, Yang Y, Liu Y, Song C. Mechanisms and characteristics of spatter generation in SLM processing and its effect on the properties. Mater Des 2017;117:121–30. https://doi.org/10.1016/j.matdes.2016.12.060.

[23] Qiu C, Panwisawas C, Ward M, Basoalto HC, Brooks JW, Attallah MM. On the role of melt flow into the surface structure and porosity development during selective laser melting. Acta Mater 2015;96:72–9. https://doi.org/10.1016/j.actamat.2015.06.004.

[24] Raza A, Schwerz C, Pauzon C, Nyborg L, Hryha E. Effect of layer thickness on spatters oxidation of Hastelloy X alloy during powder bed fusion-laser beam processing. Powder Technol 2023;422:118461. https://doi.org/10.1016/j.powtec.2023.118461.

[25] Wang D, Ye G, Dou W, Zhang M, Yang Y, Mai S, Liu Y. Influence of spatter particles contamination on densification behavior and tensile properties of CoCrW manufactured by selective laser melting. Opt Laser Technol 2020;121:105678. https://doi.org/10.1016/j.optlastec.2019.105678.

[26] He X, Kong D, Zhou Y, Wang L, Ni X, Zhang L, Wu W, Li R, Li X, Dong C. Powder recycling effects on porosity development and mechanical properties of Hastelloy X alloy during laser powder bed fusion process. Addit Manuf 2022;55:102840. https://doi.org/10.1016/j.addma.2022.102840.

[27] Bircher BA, Meli F, Küng A, Thalmann R. Metrological X-ray computed tomography at sub-micrometre precision. Geneva, Switzerland: Euspen's 20th Int. Conf. Exhib.; 2020. p. 1–4.

[28] Bircher BA, Meli F, Küng A, Thalmann R. A geometry measurement system for a dimensional cone-beam CT. 8th Conf. Ind. Comput. Tomogr. Wels, Austria (ICT 2018) 2018:1–7.

[29] Bachmann F, Hielscher R, Schaeben H. Texture analysis with MTEX – free and open source software toolbox. Solid State Phenom 2010;160:63–8. https://doi.org/10.4028/WWW.SCIENTIFIC.NET/SSP.160.63.

[30] Schwerz C, Nyborg L. Linking in situ melt pool monitoring to melt pool size distributions and internal flaws in laser powder bed fusion. Met 2021;11:1856. https://doi.org/10.3390/MET11111856. 11 (2021) 1856.

[31] Raza A, Pauzon C, Goff SD, Hryha E. Effect of processing gas on spatter generation and oxidation of TiAl6V4 alloy in laser powder bed fusion process. Appl Surf Sci 2023;613:156089. https://doi.org/10.1016/j.apsusc.2022.156089.

[32] Shaji Karapuzha A, Fraser D, Zhu Y, Wu X, Huang A. Effect of solution heat treatment and hot isostatic pressing on the microstructure and mechanical properties of Hastelloy X manufactured by electron beam powder bed fusion. J Mater Sci Technol 2022;98:99–117. https://doi.org/10.1016/J.JMST.2021.04.059.

[33] Wang G, Ouyang H, Fan C, Guo Q, Li Z, Yan W, Li Z. The origin of high-density dislocations in additively manufactured metals. Mater. Res. Lett. 2020;8:283–90. https://doi.org/10.1080/21663831.2020.1751739.

[34] Soltani-Tehrani A, Isaac JP, Tippur HV, Silva DF, Shao S, Shamsaei N. Ti-6Al-4V powder reuse in laser powder bed fusion (L-PBF): the effect on porosity, microstructure, and mechanical behavior. Int J Fatig 2023;167:107343. https://doi.org/10.1016/j.ijfatigue.2022.107343.

[35] Wu Z, Wu S, Duan Y, Huang K, He W, Du D, Dong A. In situ X-ray tomography of fracture behaviour in low-porosity L-PBF AlSi10Mg alloy with laser shock peening. Virtual Phys Prototyp 2023;18. https://doi.org/10.1080/17452759.2023.2273955.

[36] Snell R, Tammas-Williams S, Chechik L, Lyle A, Hernández-Nava E, Boig C, Panoutsos G, Todd I. Methods for rapid pore classification in metal additive manufacturing. JOM 2020;72:101–9. https://doi.org/10.1007/s11837-019-03761-9.

[37] Molaei R, Fatemi A, Sanaei N, Pegues J, Shamsaei N, Shao S, Li P, Warner DH, Phan N. Fatigue of additive manufactured Ti-6Al-4V , Part II : the relationship between microstructure. material cyclic properties , and component performance Theory of Critical Distance 2020;132. https://doi.org/10.1016/j.ijfatigue.2019.105363.

[38] Snow Z, Cummings C, Reutzel EW, Nassar A, Abbot K, Guerrier P, Kelly S, McKown S, Blecher J, Overdorff R. Analysis of factors affecting fatigue performance of HIP'd laser-based powder bed fusion Ti–6Al–4V coupons. Mater Sci Eng, A 2023;864. https://doi.org/10.1016/j.msea.2022.144575.

[39] Rafi HK, Karthik NV, Gong H, Starr TL, Stucker BE. Microstructures and mechanical properties of Ti6Al4V parts fabricated by selective laser melting and electron beam melting. J Mater Eng Perform 2013;22:3872–83. https://doi.org/10.1007/s11665-013-0658-0.

[40] Sadeghi E, Karimi P, Esmaeilizadeh R, Berto F, Shao S, Moverare J, Toyserkani E, Shamsaei N. Progress in Materials Science A state-of-the-art review on fatigue performance of powder bed fusion-built alloy 718. Prog Mater Sci 2023;133:101066. https://doi.org/10.1016/j.pmatsci.2022.101066.

[41] Pilgar CM, Fernandez AM, Segurado J. Microstructure sensitive fatigue life prediction model for SLM fabricated Hastelloy-X. Int J Fatig 2023;168:107372. https://doi.org/10.1016/j.ijfatigue.2022.107372.

[42] Sheridan L, Gockel JE, Scott-Emuakpor OE. Stress-defect-life interactions of fatigued additively manufactured alloy 718. Int J Fatig 2021;143. https://doi.org/10.1016/j.ijfatigue.2020.106033.

[43] Zhang M, Sun CN, Zhang X, Goh PC, Wei J, Hardacre D, Li H. Fatigue and fracture behaviour of laser powder bed fusion stainless steel 316L: influence of processing parameters. Mater Sci Eng, A 2017;703:251–61. https://doi.org/10.1016/J.MSEA.2017.07.071.

[44] Sanaei N, Fatemi A. Analysis of the effect of internal defects on fatigue performance of additive manufactured metals. Mater Sci Eng, A 2020. https://doi.org/10.1016/j.msea.2020.139385.